Research Square

Preprints are preliminary reports that have not undergone peer review.
They should not be considered conclusive, used to inform clinical practice,
or referenced by the media as validated information.

NCX-IP3R Crosstalk Maintains Calcium Oscillations to Regulate Angiogenic Signaling in Endothelial Cells

Donny Hanjaya-Putra

dputra1@nd.edu

University of Notre Dame https://orcid.org/0000-0002-5403-544X

Donghyun Jeong

University of Notre Dame

Stephen Cini

University of Notre Dame

Kailee Mendiola

University of Notre Dame

Satyajyoti Senapati

University of Notre Dame https://orcid.org/0000-0001-7999-1561

Alexander W. Dowling

University of Notre Dame https://orcid.org/0000-0001-9383-7499

Hsueh-Chia Chang

University of Notre Dame https://orcid.org/0000-0003-2147-9260

Jeremiah Zartman

University of Notre Dame https://orcid.org/0000-0001-7195-7203

Article

Keywords:

Posted Date: September 23rd, 2026

DOI: https://doi.org/10.21203/rs.3.rs-10475604/v1

License: This work is licensed under a Creative Commons Attribution 4.0 International License.
Read Full License

Additional Declarations: There is **NO** Competing Interest.

NCX-IP_3R Crosstalk Maintains Calcium Oscillations to Regulate Angiogenic Signaling in Endothelial Cells

Donghyun Paul Jeong[1,2], Stephen Cini[3], Kailee Mendiola[1,2], Satyajyoti Senapati[3], Alexander Dowling[3], Hsueh-Chia Chang[1,2,3,4,*], Jeremiah Zartman[1,2,3,4,5 *], Donny Hanjaya-Putra[1,2,3,4,5, *]

[1] Bioengineering Graduate Program, University of Notre Dame, Notre Dame, IN 46556

[2] Aerospace and Mechanical Engineering, University of Notre Dame, Notre Dame, IN 46556

[3] Chemical and Biomolecular Engineering, University of Notre Dame, Notre Dame, IN 46556

[4] Harper Cancer Research Institute, University of Notre Dame, Notre Dame, IN 46556

[5] Center for Stem Cell and Regenerative Medicine, University of Notre Dame, Notre Dame, IN 46556

*** Address correspondence to:**

dputra1@nd.edu,

jzartman@nd.edu,

hchang@nd.edu

Abstract

Blood endothelial cells regulate angiogenesis through calcium oscillations that coordinate migration and proliferation, yet the mechanisms governing these signaling dynamics remain poorly understood and difficult to manipulate for tissue regeneration. Here, we combine computational analysis, microfluidic electrical stimulation, and mathematical modeling to demonstrate that sodium-calcium crosstalk between the sodium-calcium exchanger (NCX) and inositol trisphosphate receptor (IP_3R) is a key regulatory mechanism of endothelial calcium oscillations and downstream angiogenic responses. We show that characteristic endothelial calcium oscillations emerge when maximal NCX-mediated calcium efflux and IP_3R-mediated calcium influx are aligned at similar intracellular calcium concentrations, producing prolonged low-calcium quasi-steady states punctuated by rapid calcium spikes. This oscillatory behavior can be modulated through pharmacological inhibition, changes in extracellular sodium, or growth factor signaling. We further identify distinct transient and sustained calcium signaling patterns associated with angiogenesis that can be recapitulated by electrical stimulation, activating angiogenic gene expression, and vascular network formation without exogenous growth factor supplementation. Together, these findings establish NCX-IP_3R crosstalk as a fundamental interaction governing endothelial calcium signaling and introduce precise control of ionic dynamics as a strategy for engineering angiogenic responses with applications in regenerative medicine.

Abbreviations

BEC	Blood Endothelial Cells
dEC	Differentiated Endothelial Cells
iPSC	Induced Pluripotent Stem Cells
ER	Endoplasmic Reticulum
NCX	Sodium-Calcium Exchange Transporter
IP_3R	Inositol 1,4,5-trisphosphate receptor
VEGF	Vascular Endothelial Growth Factor
AKT	Protein Kinase B
WNT5a	Wnt-Family Protein 5a
MAPK	Mitogen-activated Protein Kinase
K_m	Michaelis-Menten constant for calcium with IP_3R
K_i	Inhibitor constant for calcium with IP_3R
k_{NCX}	Rate constant of NCX transporter
k_{PMCA}	Rate constant of PMCA calcium pump
N_{ext}	External sodium concentration
k_s	Rate constant of sodium pump

1. Introduction

Intracellular calcium signaling plays a crucial role in many key cellular processes, such as proliferation, apoptosis, metabolism, secretion, gene regulation, and cell motility.[1–4] In response to external signals, cells are capable of drastically increasing the flux of calcium ions from either the extracellular space or intracellular calcium storage in organelles such as the endoplasmic reticulum (ER).[5,6] Calcium signaling is a ubiquitous aspect of many intracellular communication pathways because of a large set of signals, receptors, and transporters, together known as the “calcium signaling toolkit”, that can be applied to multiple cellular processes.[7,8]

Depending on the biological context, calcium-based signaling works at time scales in the order of milliseconds to minutes, allowing rapid fluctuations in calcium signaling. For example, excitable cells, such as cardiomyocytes, neurons, and muscle cells, exhibit frequencies between <1 and 100 Hz.[9,10] At longer time scales, calcium concentration dynamics can regulate gene expression in cells.[11] Interestingly, even some non-excitable cells such as endothelial cells can undergo sharp calcium oscillations similar to excitable cells in the frequency range of between 0.1 and 0.001 Hz.[9]

Because calcium activity is transitory and occurs across a broad range of frequency domains, imaging-based calcium measurements are commonly used to map out calcium dynamics. Calcium indicators, such as Fura-2 dye, result in an excitation shift or fluorescence intensity when bound to calcium.[12] Alternatively, reporter cell lines expressing a genetically encoded calcium indicator exhibit a fluorescence shift with calcium concentration fluctuations. Overall, calcium measurements rely on fluorescent imaging-based techniques of live cells imaging at high sampling rates. Understanding

calcium signaling is especially important in tissue engineering and other bioengineering applications that focus on population-wide cell communication. Calcium, in addition to playing important roles in intracellular signaling, also serves as an intercellular communication tool in many cells, aiding in spontaneous self-organizational behavior of cells often seen in organogenesis.[8,13–15]

In constructing engineered tissues, spontaneous self-organization is often the only way to form structures such as microvasculature that are smaller than the minimum spatial resolution of devices such as 3D bioprinters.[16] To induce self-organization, a heterogeneous cell population can be seeded onto a matrix and stimulated with relevant growth factors.[17–21] Cells can respond to mechanical stimuli such as shear stress, chemical gradients of nutrients and growth factors, or contextual cues such as the presence of other neighboring cells.[22–24] In fact, numerous studies have indicated that the spatial distribution and intercellular communication play crucial roles in the self-organization of the cells into functional tissues.[25–27]

This calcium signaling toolkit is especially relevant in vascular tissue engineering. Calcium spiking plays a crucial role in directing endothelial cellular response to various external stimuli, such as growth factors, mechanical forces, or metabolic stresses, that are present in a vascular system.[28] For example, shear stress is known to induce cytoplasmic calcium spiking with a response time in the range of 1 minute in blood and lymphatic endothelial cells.[29–31] Endothelial cells also exhibit repeated calcium oscillations in response to reoxygenation following a period of hypoxic stress.[32] Of special relevance to tissue engineering applications is the calcium-mediated endothelial response to pro-angiogenic growth factors. In particular, vascular endothelial growth factor (VEGF)

induces physiologically relevant responses in endothelial cells, such as proliferation and migration, that define angiogenesis.[33–35] Previous studies have demonstrated that VEGF induces calcium signaling dynamics via amplitude modulation or frequency modulation.[36] However, due to the lack of high-throughput, robust methods for collecting quantitative calcium data, combined with the high degree of heterogeneity in spiking behavior among endothelial cells, it remains difficult to obtain quantitative measurements of subtle frequency shifts in response to external stimuli.

Therefore, there is a need for a better understanding of how calcium dynamics in large non-excitable cell populations affect angiogenesis. Using newly developed computational analysis tools, we identified a previously uncharacterized calcium-signaling mechanism that modulates endothelial responses to angiogenic growth factors. We quantify key metrics describing endothelial responses to VEGF and reproduce these effects through controlled external ionic levels using a novel microfluidic device. These experimental data are used to tune a mathematical model based on sodium-calcium exchanger and IP_3R-mediated calcium fluxes that captures endothelial calcium oscillations, which we then use to predict cellular responses to new external perturbations and thereby create a feedback loop between experiments and simulations **(Figure 1)**. Altogether, our study demonstrates that controlling calcium signaling dynamics through ionic depletion can serve as a versatile method for generating angiogenic responses in engineered tissue constructs for various applications in tissue engineering and regenerative medicine.

2. Results

2.1 Endothelial cells exhibit a robust acute and chronic calcium response to VEGF

We first designed an efficient computational pipeline to characterize calcium dynamics in endothelial cells using live fluorescence microscopy. We stained blood endothelial cells (ECs) with calcium-sensitive Calbryte 520AM dye, which increases in fluorescence brightness when bound to cytosolic calcium. Very briefly, the pipeline performs segmentation to identify the boundary of each cell, calculates the average fluorescence intensity within each cell, and then extracts calcium dynamics features such as frequency or cross-correlation (**Supplementary Figure S1**).

Using this pipeline, we captured the response of ECs to VEGF at two different timeframes: an acute response, which happens within seconds of VEGF stimulation, and a chronic response, which occurs in the order of hours. First, the addition of VEGF causes an immediate wave of calcium spikes that propagate through the endothelial population within seconds **(Figure 2A, Supplemental Movie S1)**. We estimate this wavefront of calcium spike activity propagates at an approximate rate of 2400 μm/min, calculated using the timepoints at which cells across the imaging window reached maximum calcium intensity **(Figure 2B)**. This rapid propagation indicates that the wavefront is independent from diffusion of VEGF molecules, which has an expected diffusive velocity in the order of 10^2 μm/min, assuming a diffusivity of 10^{-6} cm^2/s over a few cm of the imaging window. Therefore, we hypothesized that the VEGF-mediated wave propagation is most likely due to intercellular exchange of ions (e.g., through gap junctions) rather than VEGF diffusion.

We next quantified the degree of synchronization by measuring the cross-correlation values for each cell-cell pair within the imaging window. Cross-correlation values were calculated assuming no temporal shifts. When VEGF-stimulated cells were compared with non-stimulated cells, we observed a clear shift toward higher synchronization, with the number of cell-cell pairs exhibiting a cross-correlation value of at least 0.5 increasing from around 50% to nearly 100% **(Figure 2C-D, Supplementary Figure S4)**.

We then collected calcium measurements 24 hours after exposure to VEGF and measured the average spiking frequency for each cell exhibiting oscillatory behavior. In a non-stimulated condition of less than 0.5 ng/mL VEGF, the cells exhibited an average spiking frequency of approximately 8 mHz (Figure **2D, F, Supplementary Movie S2)**. This spiking frequency shifted to approximately 12 mHz with the addition of 50 ng/mL of VEGF **(Figure 2E, F, Supplementary Figure S2, Supplementary Movie S3)**. This pattern was conserved with treatment as low as 10 ng/mL VEGF, with no dose-dependent changes in frequency, suggesting that VEGF-activated frequency shift is a highly sensitive stepwise activation mechanism **(Supplementary Figure S3).**

Interestingly, we also found that induced pluripotent stem cell (iPSC)-derived endothelial cells exhibit this same frequency as they reach terminal differentiation. Human iPSCs are typically differentiated to endothelial cells through a stepwise treatment involving various growth factors, followed by maturation into mature endothelial cells through VEGF treatment.[37–39] We differentiated hiPSCs to endothelial cells using an 8-day stepwise protocol and measured calcium spiking frequencies at day 6 and day 8. As expected, at day 6, the immature differentiated endothelial cells (dEC) exhibited a low

spiking frequency of around 8 mHz even in the presence of 50 ng/mL of VEGF **(Figure 2G, I, Supplementary Movie S4)**. In contrast, fully matured dECs at day 8 exhibited a 11 mHz spiking frequency, which matched the response of the native blood endothelial cells in the presence of VEGF **(Figure 2H, I, Supplementary Movie S5)**. These results suggest that spiking frequency response defines the degree of maturity of hiPSC-derived ECs.

2.2 Ion depletion and electrical stimulation directly induce acute calcium responses in ECs

To show that we can mimic the effects of VEGF through regulation of external ionic concentration, we devised a microfluidic channel equipped with a selectively permeable ionic membrane (SPIM), which has been shown to deplete ions in a cell culture.[40] We modified a single-channel fluidic chip with two wells by inserting a narrow pipette tip within one of the wells **(Figure 3A)**. The pipette tip was modified by inserting the SPIM into the narrow opening such that the membrane fully separates the inner pipette chamber and the outer well of the chip. Then, a negative electrode was placed inside the media in the pipette tip, and a positive electrode was placed in the outer well. When the current was applied, we confirmed that the charged dye placed inside the microfluidic channel is transferred to the pipette tip through the SPIM **(Figure 3B)**. Using this microfluidic chip, we synchronously depleted the ions present in the cell culture media, which noticeably shifted in the degree of synchronization in BEC oscillations similar to that of VEGF stimulation **(Figure 3C, Supplementary Movie S6)**.

A temporary shift in external ionic concentration hence mimics the transient effect of VEGF on cellular calcium signaling synchronization. Since external ion depletion

reduces ion flux into the cell, particularly sodium influx, an electrical current should also produce a similar effect because of the diode-like rectification feature of various unidirectional ionic pumps. Unlike global ion depletion by the SPIM around the cell, an electric current imposes a potential gradient across the cell, which induces cation efflux on one side of the cell and cation influx on the other. However, due to the nonlinear diode feature of many cation channels, the influx and efflux are not perfectly antisymmetric and a net efflux results. This net efflux due to a DC current hence has a similar effect to that induced by cation depletion by SPIM. Therefore, we devised a new microfluidic chip in which two electrodes are placed in opposing wells, and a controlled current is applied directly through the cell culture area to induce ionic current **(Figure 3D)**.

Next, we optimized the current and voltage parameters required to mimic the effect of VEGF on calcium oscillation synchronization and identified a range of 10-12 V and 4.5-5.5 mA as optimal for the system. Using these parameters, we applied a 50-second current pulse to the BECs and measured the calcium oscillation pattern during and after the pulse, where the BECs exhibited the same synchronization behavior as seen with VEGF stimulation **(Figure 3E, Supplementary Movie S7)**. Nearly 90% of cells treated with the current exhibited a cross-correlation coefficient of >0.5, which is significantly higher than non-treated controls **(Figure 3F, Supplementary Figure S4)**.

We also explored whether this current-based calcium synchronization is sufficient to replicate the physiological effects of VEGF on cells. We compared cells treated with VEGF with cells stimulated with a single 50-second electric pulse, and with unstimulated cells after 6 hours of initial stimulation by measuring the transcriptional levels of VEGF-target genes. We found that the VEGF-treated cells had elevated levels of *AKT*, *WNT5A*,

and *KDR* compared to non-VEGF-treated cells, while the current-treated cells exhibited a significantly greater upregulation of the same genes at the 6-hour timepoint compared to non-VEGF-treated cells **(Figure 3G-I)**.

In particular, *AKT* is a component of the *PI3K/AKT* pathway, regulating cellular processes such as proliferation and cell survival and is a known target of VEGF-mediated signaling.[41–45] *WNT5A* is endogenously expressed in endothelial cells and is involved in pro-angiogenic pathways.[46,47] *KDR*, or VEGFR2, is the primary receptor of VEGF in endothelial cells and is crucial for the VEGF-mediated signaling cascade.[48,49] The parallel upregulation of these genes in the current- and VEGF-treated cells indicates that current stimulation can successfully recapitulate key downstream signaling effects of VEGF.

Notably, *MAPK*, another crucial VEGF-dependent pathway, was not significantly elevated in VEGF-treated cells but was significantly elevated in current-treated cells, which may indicate a temporal delay in VEGF-*MAPK* activation pathway that the current-based calcium-mediated stimulation is able to bypass **(Figure 3J)**.[50,51] Conversely, *CTGF*, which can inhibit VEGF-induced angiogenesis, was downregulated in VEGF-treated cells, but the current-treated cells were unaffected. This finding suggests that calcium synchronization acts through a pathway specific to the VEGF signaling cascade **(Figure 3K)**.[52]

To fully confirm the pro-angiogenic effects of direct electric stimulation, we performed a commonly used tube formation assay by seeding ECs on top of Matrigel surfaces and allowing them to form networks.[53] ECs that were pre-treated with electrical current formed extensive networks within three hours of seeding, compared to non-treated ECs **(Figure 3L-M, Supplementary Figure S6)**. We quantified the network using

AutoTube, a MATLAB-based software that performs tube detection, skeletonization, and statistical analysis.[54] We found that the pre-treated cells formed significantly longer networks with more branch points, indicating that the current-treated ECs have higher angiogenic potential **(Figure 3N-O)**. Taken together, our data suggest that transient electrical stimulation or ionic depletion using microfluidic-inspired circuits mimics the effects of VEGF-induced angiogenesis by modulating intracellular calcium.

2.3 Calcium spiking couples with predicted sodium dynamics through the NCX transporter

Classical mathematical models such as the Fitzhugh-Nagumo model or the more recent Ten Tusscher model describe calcium spiking in excitable cells through rapid, coupled changes in membrane potential.[55,56] In electrically non-excitable endothelial cells, however, the membrane potential does not vary on the same timescale, necessitating a different mechanism to account for the observed oscillatory behavior **(Supplementary Movie S8)**. Because the plasma membrane is more permeable to potassium than sodium due to K-leak channels, potassium contributes more strongly to the membrane potential.[57,58] This suggests that in non-excitable endothelial cells, calcium dynamics may be coupled more closely with sodium than potassium—and the calcium dynamics are much slower than the membrane potential dynamics. We therefore hypothesized that small sodium fluctuations, coupled to calcium via sodium-calcium transporters, can generate large calcium spikes without producing comparably large changes in membrane potential.

To test this hypothesis, we measured the calcium oscillation dynamics before and after a sudden twofold increase in external sodium concentration from 140 mM to 300 mM.[59] As shown in the representative calcium concentration trace, nearly all cells abruptly

stop their oscillations just seconds after the sodium spike **(Figure 4A, Supplementary Movie S9)**. This lack of oscillation can be drastically reversed within seconds by reducing the sodium concentration to 140 mM again by diluting the media with deionized water (**Supplementary Movie S10**). In comparison, the cells continue to oscillate when the potassium concentration is increased tenfold from 5 mM to 50 mM, indicating that calcium oscillations are coupled to the sodium concentration (**Supplementary Movie S11**).

To explain these results, we hypothesized that the sodium-calcium exchanger transporter (NCX) is the most likely coupling mechanism of sodium and calcium. NCX is a widely studied ion antiporter that transports one calcium ion for every 3 sodium ions.[60] We then treated the endothelial cells with 50 μM of SEA0400, an NCX inhibitor. We found the percentage of cells undergoing oscillation decreased dramatically from around 40% to less than 2% within 20 minutes **(Figure 4B, Supplementary Movie S12)**.[61] Taken together, these results suggest that the calcium oscillations in non-excitable endothelial cells are coupled with sodium dynamics through NCX.

2.4 The near-tangency between NCX and IP_3R calcium fluxes sustains oscillatory spiking

Based on these insights, we developed a mathematical model to describe calcium spiking patterns in non-excitable cells, which do not exhibit rapid jumps in membrane potential as excitable cells do. Our model relies on our hypothesized NCX-IP_3R-dependent calcium dynamics pathway **(Figure 4C).** From our experimental observations, calcium dynamics should be faster than sodium dynamics. While these calcium dynamics are unrelated to large fluctuations in membrane potential that occur in excitable cells, the observed calcium spiking and memory phenomena suggest that hysteresis in calcium relative to sodium is at play.

We therefore modified the classical Fitzhugh-Nagumo model for potential spiking as a foundation for the calcium spiking model. While the former models rely on nonlinear hysteretic features introduced by voltage-gating of potassium channels, our model focuses on how calcium-gating of NCX and IP_3R yields the observed calcium hysteresis and spiking.

The inositol 1,4,5-trisphosphate receptor (IP_3R) is primarily responsible for the rapid release of calcium from the endoplasmic reticulum (ER).[62–64] Importantly, IP_3R exhibits a biphasic regulatory mechanism with respect to cytosolic calcium concentration (calcium-induced-calcium-release mechanism): its calcium release is activated by allosteric binding of calcium, but is inhibited at saturating concentrations of cytosolic calcium.[65–67] This widely studied mechanism of IP_3R-mediated calcium release is critical for the oscillatory behavior of calcium. We modeled the ionic flux through IP_3R with a Michaelis-Menten curve (please see **Materials and Methods** section) as shown in **Figure 4D**.

Next, we modeled the calcium efflux through the NCX transporter. In typical physiological states, the NCX transporter is driven by the sodium gradient across the cell membrane, which allows calcium ions to be depleted from the cytosol against their own concentration gradient.[68] NCX also exhibits allosteric activation by intracellular calcium through its two binding domains, CBD1 and CBD2, which increases the calcium transport rate.[69–71] However, very high levels of intracellular calcium can also reverse the NCX transport direction through autoinhibition or indirectly through calmodulin regulation or activation of the NCX-cleaving protease.[72–74] This calcium-dependent activation-inhibition is modeled using a simple bell curve (see Methods Section) as shown in **Figure 4E**.

To understand the origin of this oscillatory behavior, we performed a phase-plane analysis, examining the nullclines of the sodium and calcium dynamics. The sodium nullcline traces a parabola in the calcium-sodium (C-N) phase plane, with its maximum corresponding to peak NCX-mediated sodium influx. Oscillatory spiking arises when this sodium nullcline intersects the middle branch of the calcium nullcline's S-shaped hysteresis curve **(Figure 4F-G)**.

When the IP_3R and NCX flux optima are aligned, the parabolic sodium nullcline becomes nearly tangent to the calcium nullcline's low-C branch at its lower turning point. At this near-tangency, both calcium and sodium dynamics slow substantially: calcium remains low while sodium accumulates gradually. On the high-C branch, by contrast, the two nullclines are well-separated, and the resulting faster dynamics constitute the spike itself. Because tangency between the nullclines occurs only within a narrow, finely tuned parameter regime, the spike interval should be sensitive to parameter perturbation, while the spike itself, governed by the well-separated high-C branch, should be comparatively robust. This is confirmed by our sensitivity analysis: peak height is largely insensitive to parameter changes, whereas oscillation frequency is highly sensitive **(Figure 4H)**.

This oscillatory regime depends specifically on the IP_3R and NCX flux curves having closely matched peak magnitudes, with the IP_3R-mediated calcium flux peaking at a slightly lower calcium concentration than the NCX-mediated efflux **(Figure 4I)**. This near-tangency between the NCX efflux and IP_3R influx curves is what sustains the oscillatory system: only a small perturbation in calcium concentration is needed to trigger the rapid IP_3R-mediated influx, producing a transient calcium buildup that is subsequently cleared by the comparatively slower NCX-mediated efflux. The resulting low-C interval,

during which the ER remains dormant between spikes, is therefore governed by the bandwidth and amplitude of the IP_3R and NCX flux maxima, which in turn reflect the number and calcium-binding affinity of the regulatory sites on each protein.

2.5 Perturbations experiments validate multiple predictions generated by the null-cline tangency model

We verified that this null-cline tangency model, due to alignment of calcium concentrations with high ER and NCX fluxes, explain the experimental results we have discussed previously **(Figure 5A)**. It is known that VEGF primarily affects calcium signaling through IP_3R. We demonstrated that the frequency of the calcium oscillation can be increased solely by modifying the $\frac{1}{K_i}$ parameter from 3 to 3.3 **(Figure 5B)**. IP_3 modulates IP_3R-calcium release by inducing conformational changes that affect the allosteric calcium binding, which concurs with the model prediction that lower allosteric inhibitory calcium-IP_3R binding will increase the spiking frequency.[75] This change in frequency is represented by a leftward shift in the peak of the IP_3R-flux curve, which pushes the system into the higher-frequency zone, indicating that the cells can modulate the oscillatory frequency by altering the relative peak locations of the NCX and IP_3R fluxes **(Figure 5C)**.

We also verified that the model exhibits the same calcium dynamics we observed with external sodium concentration modulation. First, when we adjust the external sodium concentration from 30 to 28, we see that the oscillation pattern is maintained, but crucially, there is a period of sustained high calcium concentration, which is followed by continued oscillation **(Figure 5E)**. This temporary high-calcium state corresponds to when the NCX

flux briefly turns negative due to the sudden decrease in external sodium as the driving force, indicating that NCX briefly enters reverse mode **(Figure 5F)**. This reflects the behavior of endothelial cells during external cation depletion **(Figure 5D)**. Additionally, a previous study reported that reverse-mode NCX is required for calcium activity and angiogenic activation in ECs in a low-external sodium environment, which corroborates our findings here.[76]

We also verified that the sudden spike in external sodium from 30 to 38 can lead to a sudden stop of oscillations and the cells being stuck in the "low calcium" state, as the NCX flux increases drastically to pump out calcium before it can accrue in the cytosol due to the increase in sodium concentration gradient **(Figure 5H-I)**. This again matches the experimental data from external sodium spiking **(Figure 5G)**.

Lastly, when we introduce to the system, which already lacks oscillation due to high external sodium $N_{ext} = 35$, the $\frac{1}{K_i}$ parameter change from 3 to 3.3 simulating VEGF addition, the model predicts a resumption of oscillation as the leftward shift of the IP_3R-flux curve lowers the required calcium level to trigger the IP_3R calcium release, allowing the oscillation to occur even with increased calcium efflux from NCX (**Figure 5K-L**). We experimentally validate this by introducing 50 ng/mL of VEGF into a cell population with the external sodium spiked to 250 mM while keeping the sodium concentration constant. This results in the resumption of oscillatory activity, validating the model predictions (**Figure 5J, Supplementary Movie S13**).

3. Discussion

Intracellular calcium dynamics are a fundamental signaling mechanism that regulates diverse cellular processes across eukaryotic cell types.[77,78] Calcium signaling spans a wide range of spatiotemporal patterns, from local puffs to intercellular waves.[79] While electrically non-excitable, endothelial cells exhibit variable spatiotemporal calcium signaling activity that depends on IP_3 receptor (IP_3R)-dependent calcium release from the endoplasmic reticulum.[80] These oscillations play a critical role in regulating endothelial behaviors such as angiogenesis, yet their complexity has made population-scale analysis challenging.[81–83] Consequently, how endothelial calcium dynamics are modulated by external stimuli has remained poorly understood.

To address this challenge, we developed a computational-experimental pipeline that robustly quantifies calcium oscillation features, including frequency and cross-correlation, across large endothelial populations. Using this approach, we identified distinct transient and chronic responses to VEGF stimulation: endothelial cells rapidly synchronize within seconds of VEGF exposure before transitioning to a sustained increase in oscillation frequency. Building on this observation, we developed a microfluidic platform that manipulates extracellular ionic conditions and showed that electrical stimulation induces calcium synchronization resembling the VEGF response, resulting in upregulation of pro-angiogenic genes and enhanced endothelial cell network formation. Together, these findings demonstrate that endothelial calcium signaling can be directly manipulated through electrical cues, providing a strategy for precise spatiotemporal control of angiogenic signaling that could complement or reduce reliance on exogenous growth factor delivery.

Inspired by these results, we hypothesized that calcium oscillations are coupled with sodium ions in ECs. To evaluate this hypothesis systematically, we developed a mathematical model based on mechanisms of the NCX transporter and IP_3R-based calcium release from the endoplasmic reticulum and found that our model creates oscillatory calcium patterns consistent with what we observed experimentally. We then confirmed that the model accurately predicts EC responses to various external stimuli, such as VEGF stimulation and external ion depletion or supplementation, demonstrating the potential value of our proposed IP_3R-NCX model for explaining calcium behavior in endothelial cells.

Although mathematical models such as Hodgkin-Huxley and FitzHugh-Nagumo have successfully described calcium dynamics in excitable cells, they rely on strong coupling between membrane potential and calcium flux, making them less applicable to non-excitable endothelial cells. Previous studies have independently implicated both IP_3R and NCX in endothelial calcium regulation, but none have described how their interaction generates sustained calcium oscillations or links these dynamics to angiogenic signaling.[76,84–86] Our model addresses this gap by demonstrating that oscillations emerge from the coupled activation-inhibition kinetics of NCX and IP_3R rather than membrane potential. The model also explains how rapid calcium oscillations can occur without large fluctuations in intracellular sodium or membrane voltage, consistent with experimental observations, and accurately predicts cellular responses to multiple perturbations.

Our model provides mechanistic insight into how endothelial cells regulate calcium oscillations to drive angiogenic responses. Specifically, we show that near-alignment between the maximum calcium efflux mediated by NCX and the maximum calcium influx

through IP_3R is required to generate the characteristic oscillatory pattern observed in endothelial cells, consisting of prolonged quasi-steady periods of low cytosolic calcium punctuated by brief calcium spikes. This oscillatory behavior can be tuned by shifting the activation-inhibition properties of NCX, IP_3R, or both, through mechanisms such as VEGF signaling, changes in extracellular sodium concentration, or electrical current. Together, these findings suggest that endothelial cells maintain a finely balanced calcium oscillatory state that enables rapid yet sustained responses to external stimuli, providing a new mechanistic framework for understanding calcium signaling in endothelial biology.

In summary, we demonstrate that endothelial cells encode angiogenic signals through coordinated changes in calcium oscillation frequency and synchronization. By combining quantitative calcium analysis, electrical stimulation, and mathematical modeling, we show that VEGF-like signaling can be reproduced by directly manipulating ionic dynamics. Our near-tangent nullcline model provides a mechanistic framework for understanding endothelial calcium oscillations and offers predictive capability for responses to pharmacological or electrical perturbations. Together, these findings establish endothelial calcium dynamics as an engineerable signaling modality with potential applications in tissue engineering, regenerative medicine, and vascular biology research.

4. Materials and Methods

Human iPSC and BEC Culture

Human BECs derived from the dermis of an adult donor (Promocell) were expanded and used between passages 5 and 8. The cells were cultured in MV2 media (Promocell) and incubated at 37°C with 5% CO_2. IMR90, human iPSCs derived from lung fibroblast (WiCell) were seeded on tissue culture plastic surfaces coated with 0.083 mg/mL of Matrigel (Corning) in DMEM-F12 media (Gibco) and grown in mTeSR+ media (Stem Cell Technologies) at 37°C with 5% CO_2. 10 μM of Y-27632 Rho-kinase inhibitor was added to the cell culture media for the first day after seeding, then subsequently removed. All cell lines were routinely tested for mycoplasma contamination and were negative throughout this study.

Automated computational pipeline for large-scale calcium oscillation data extraction in non-excitable cells

We designed a data processing pipeline to analyze intracellular calcium oscillation patterns in non-excitable cells **(Supplementary Figure S1A-C)**. The overall pipeline receives the raw fluorescent image stack at a magnification between 4 and 10x in TIFF. format. These images capture the fluorescent signal intensities of the mesodermal-lineage cells, which correspond to cytoplasmic calcium concentration. For this study, we relied on Calbryte 520AM dye, a robust calcium indicator dye that is non-fluorescent until bound with calcium ions within the cell.

Before proceeding with the pipeline, the images require preprocessing **(Supplementary Figure S1A)**. This process begins with a rolling ball background

subtraction to remove the effects of uneven background signal. It is followed by a despeckle step to remove the signals attributed to non-cellular fragments. Next, a dead cell detection step identifies and excludes auto-fluorescent dead cells by setting a maximum fluorescence intensity threshold. The processed images are then segmented using a Cellpose-based algorithm. This segmentation is performed on the max-projection image generated from the entire image stack, with optional image drift correction applied as needed. The resulting segmentation masks are used to generate the average intensities for each cell at every timepoint, which is saved to an intensity (n-by-t) matrix, where n is the number of identified cells and t is the total number of timepoints.

After preprocessing the image stack, the next step is data processing **(Supplementary Figure S1B)**. The extracted data is then processed individually by fitting a 6^{th}-order polynomial to each time series data, then subtracting the values from the fitted polynomial to correct for the overall background signal increase or loss of fluorescence due to photobleaching. Afterward, the cells are classified into either spiking, partial spiking, or non-spiking cells based on a peak detection algorithm, which identifies the time points at which the signature calcium spike peaks occur. The peak-thresholding parameters are set by the user based on the imaging setup and cell behavior. The pipeline takes the processed data for spiking cells and extracts parameters for subsequent analysis such as frequency shift or synchronization (**Supplementary Figure S1C**). These data can be exported and analyzed for correlation with the cell morphological or spatial information identified from the corresponding cell masks extracted from the cell segmentation step.

We demonstrate the viability of our method in detecting irregular calcium oscillation patterns in non-excitable cells. The sample images consist of human dermal blood

endothelial cells (BECs) which were cultured to confluency. They were stained with Calbryte 520AM dye without probenecid treatment to capture the calcium dynamics of cells. A resulting image at a single time point is shown with representative images of each cell type (spiking, partial spiking, or non-spiking) identified by the pipeline **(Supplementary Figure S1D)**.

We compared the results of our algorithm with the manual segmentation method, which consists of manually segmenting and identifying the spiking cells. We demonstrated that the automated method and the manual segmentation can identify approximately similar number of cells, but with greater consistency with automation **(Supplementary Figure S1E-F).** The calcium data for the two extraction methods both estimated similar oscillating periods and percentages of spiking cells, demonstrating that there is no significant difference between the two methods **(Supplementary Figure S1G-H).** Taken together, these results demonstrate that our automated algorithm can reliably capture highly irregular calcium spiking dynamics in a large cell population in a timely and non-labor-intensive manner.

Human iPSC Differentiation to BEC

Human iPSCs were seeded in a single-cell suspension at 30,000 cells/cm^2 in mTeSR+ media containing 10 μM of Y-27632 for one day. The media was switched to 4mL of APEL2 media (Stem Cell Technologies) containing 6 μM of CHIR99021 (Stem Cell Technologies) per well in a 6-well plate and allowed to differentiate for 2 days. Following this, the media was replaced with 4mL of APEL2 media containing 50 ng/mL VEGF-A (Stem Cell Technologies), 25 ng/mL BMP4 (Stem Cell Technologies), and 10 ng/mL

FGF2 (R&D Biosciences) and left for 2 days. Following this, the cells were detached using TrypLE Express (Gibco) and replated at a density of 50,000 cells/cm^2. The cells were cultured in MV2 media containing 50ng/mL of VEGF-A for up to 4 days with media change every 2 days.

Calbryte 520AM Staining and Imaging

Calbryte 520AM dye (AAT Bioquest) resuspended in DMSO was added to serum-free MV2 media at a final concentration of 5 μM. The cells were washed 1x with dPBS without calcium, then incubated with the Calbryte staining solution for 60 minutes. Following the incubation, the staining solution was removed, and the cells were washed 1x with dPBS without calcium. Fresh media was added, and the cells were imaged at 5-second intervals with a GFP excitation laser. For fluorescence imaging, either the Agilent Lionheart microscope (BioTek) or the A1R confocal microscope (Nikon) were used at 10x objectives.

Chip Design and Fabrication

A tube incorporating a buffer reservoir was fabricated by 3D printing as previously described.[87] The outer diameter of the tube was designed to match the well of a commercial single-channel ibidi chip, allowing the reservoir tube to fit tightly into the chip well. The end of the tube was shaped into a half-disk to enable attachment of a small piece of cation-exchange membrane using a UV-curable adhesive. A small hole was made at the bottom of the buffer reservoir and sealed with 2% agarose gel, ensuring that the current flowed between the buffer reservoir and the tube through the membrane when an electric field was applied. The electric field was established by connecting the positive

terminal to the buffer reservoir and the negative terminal to the tube, thereby generating a depletion front in the channel that gradually extended toward the cells.

Electrical Stimulation

Human BECs were seeded in either an Ibidi single-channel microfluidic chip (Ibidi) or a 6-well plate and allowed to reach 100% confluency. SourceMeter 2400 source measure unit (Keithley) was used to generate the electrical pulse current. The electrodes were placed on either end of the channel for the microfluidic chip, or on the opposite edges of the well in a 6-well plate. Voltage values were held constant between 10-12 V, and the current reached 10-12 mA across the Ibidi chip. Since the well plate experiences different resistance depending on the volume of cell culture media, we empirically tested various media volumes until we determined the correct volume to reach the same resistance across the well as the Ibidi chip, at 950μL of MV2 media. The chip or the well plate connected to the electrode was placed inside the Agilent Lionheart microscope's incubation chamber, and the imaging was started at least 5 minutes prior to applying the electrical stimulation to measure the transient effects.

Gene Expression

To analyze gene expression, we collected the RNA from BECs using a Qiagen Mini-prep kit (Qiagen) and quantified and diluted to the same concentration for all samples. The RNA was reverse transcribed using a high-capacity cDNA reverse transcription kit (Thermo Fisher) following the manufacturer's recommended protocol. We used TaqMan gene expression assays (Thermo Fisher) following manufacturer protocols and used GAPDH as endogenous controls to normalize relative gene expression levels using the

567 $\Delta\Delta C_T$ method (**Supplementary Table 1**). All statistical analysis was done on the $\Delta\Delta C_T$
568 values.

569 *Matrigel Angiogenesis Assay*

570 Growth-factor reduced Matrigel (Corning) was thawed on ice and quickly pipetted
571 into the inner well of the μ-Slide Angiogenesis slide (Ibidi) at a volume of 10 μL per well.
572 The slide was placed into the incubator at 37°C for 30 minutes to allow for crosslinking.
573 The cells were treated with electrical current, live-stained with 5μM of Celltracker Green
574 Dye CFMDA (Thermo Fisher) for 20 minutes, then passaged and counted. The cells were
575 resuspended at 200,000 cells/mL in MV2 media, and 50μL of the cell suspension was
576 added on top of the polymerized Matrigel inside the μ-Slide well. The cells were allowed
577 to settle for 1 hour and imaged every hour afterwards.

578 *Derivation of the model*

579 We start with the previously mentioned IP3R mechanics, which exhibits allosteric
580 activation and inhibition from intracellular calcium. Here, we model this behavior using
581 simple substrate-inhibitory Michaelis-Menten kinetics. The calcium flux through IP_3R is
582 defined as a function of cytosolic calcium as shown here:

583 $$J_{IP3R} = \frac{kC}{1 + \frac{C^2}{K_i} + \frac{C}{K_m}}$$

584 where k is the rapid ER calcium release kinetic constant, and K_m and K_i are the
585 association equilibrium constants of calcium binding for transport and substrate inhibition.
586 The biphasic mechanism produces an optimum calcium concentration at $C = \sqrt{K_i}$ for

maximum calcium ER release rate, and the bandwidth of calcium concentration around this highest calcium release rate is governed by $\frac{1}{\sqrt{K_i}}$.

Next, we modeled the calcium efflux through the NCX transporter, which also exhibits similar activation-inhibition with respect to intracellular calcium. We model this behavior through a simple bell curve with the peak transport rate achieved at a set threshold of calcium concentrations and the transport rate driven by the sodium gradient. The rate of calcium flux through NCX is defined as follows:

$$J_{NCX} = k_{NCX} e^{-\left(\frac{C-C_K}{K_a}\right)^2} (N_{ext} - N)$$

where C_K represents the critical concentration of calcium at which the maximum NCX transport rate is reached, and K_a represents the rate at which calcium binding to the allosteric activation and inhibition sites is achieved. As a matter of convenience, the NCX flux is denoted as positive when calcium is in efflux, corresponding to the forward mode of NCX. This calcium/sodium efflux/influx rate has a maximum at an intracellular calcium concentration of $C = C_k$.

We further include a simple transport rate constant for the plasma membrane calcium pump (PMCA), which is capable of pumping calcium at a low but steady rate even at low calcium concentrations driven by ATP.[88] Therefore, we propose the following two equations for the dynamics of the intracellular calcium concentration C and the intracellular sodium concentration N:

$$\frac{dC}{dt} = \Lambda\left(\frac{kC}{1 + \frac{C^2}{K_i} + \frac{C}{K_m}} - k_{PMCA} C - k_{NCX} e^{-\left(\frac{C-C_K}{K_a}\right)^2} (N_{ext} - N) + g\right)$$

$$\frac{dN}{dt} = 3k_{NCX}e^{-\left(\frac{C-C_K}{K_a}\right)^2}(N_{ext} - N) - k_sN + d(N_{ext} - N)$$

where *d* represents the concentration gradient-driven rate of sodium leakage across the plasma membrane and g represents a constant calcium leakage from the ER.[89] The k_sN term represents the voltage-dependent sodium-potassium pump, which effectively behaves as a one-way diode current rectifier, given that they are non-reversible.[90–93] This allows the cells to remain sensitive to externally applied electrical current, similar to our observations in **Figure 3E**.

The nullcline of the Calcium dynamics in the C-N phase plane produces an S-hysteresis with respect to the intracellular sodium concentration *N*, with a high-C branch and a low-C branch connected via a middle branch **(Figure 4F-G)**. The high-C turning point corresponds to the NCX optimum calcium efflux, and the low-C turning point corresponds to the ER optimum calcium release. The calcium dynamics undergo discontinuous jumps at these two turning points.

Due to binding-induced calcium buffering, the cytosolic sodium concentration *N* is significantly higher than that of the calcium *C*. Hence, the sodium flux terms must nearly cancel each other in the dynamics for the sodium ion to produce slow dynamics. Consequently, the related kinetic constants k_{NCX}, k_s, and *d* should all be unit order with respect to *N*. However, this cancellation is not possible for the calcium dynamics unless the kinetic constants *k*, k_{PMCA} and *g* are of comparable order as *N*.

In the above dimensionless equations, we have scaled these fast calcium kinetic parameters to unity order and introduced a stiff parameter $\Lambda \gg 1$. A value of $\Lambda = 2000$ is used for all our computations. This stiff parameter produces fast calcium dynamics due

to coupling with NCX, with coordinated 3:1 large sodium flux and a large ER calcium release rate, both with actual rates much higher than the sodium pump and sodium leakage.

Nondimensionalization of the model

Consider the dimensional equation for calcium and sodium below.

$$\frac{dC'}{dt'} = \frac{k'C'}{1 + \frac{C'}{K_m'} + \frac{C'^2}{K_i'}} + g' - k_{PMCA}'C' - k_{NCX}'(N_0' - N')f(C')$$

$$\frac{dN'}{dt} = 3k_{NCX}'(N_0' - N')f(C') + d'(N_0' - N') - k_s'N'$$

We note k_s has units of inverse time. Since all the fluxes for sodium should be the same order and unit order with respect to the Calcium fluxes, we can choose $1/k_{s*}$ as the characteristic time. We define $t' = \frac{t}{k_{s*}}$, $C = C'/C_*$, $N_0 = N_0'/N_*$, $N = N'/N_*$, $k_s = \frac{k_s'}{k_{s*}}$ where the unprimed quantities are dimensionless. Typical values we observe would be $C_* = 1\,\mu M$, and $N_* = 5 - 10\,mM$, making $\Lambda = \frac{N_*}{C_*} = 5000 - 10{,}000$. Then, the sodium equation becomes

$$\frac{dN}{dt} = 3k_{NCX}(N_0 - N)f(C) + d(N_0 - N) - k_sN$$

where $(k_{NCX}'/k_{s*}) = k_{NCX}$ and $d = \frac{d'}{k_{s*}}$ are all unit order dimensionless parameters.

The calcium gating function for NCX is $f(C) = e^{-\left(\frac{C - C_k}{k_a}\right)^2}$ where we have used $C = C'/C_*$, $C_k = C_k'/C_*$, and $k_a = k_a'/C_*$. Using the same scaling, we get

$$\frac{dC}{dt} = \frac{(k'/k_{s*})C}{1 + \frac{C}{K_m} + \frac{C^2}{K_i}} + (g'/C_* k_{s*}) - (k'_{PMCA}/k_{s*})C - (k_{NCX} N_*/C_*)(N_0 - N) f(C)$$

We note that the large $\Lambda = N_*/C_*$ term that appears in the NCX flux term for calcium does not appear in the sodium *N* equation. To balance this term, all the other dimensionless flux kinetic coefficients $\frac{k'}{k_{s*}}$, $(g'/C_* k_{s*})$, and (k'_{PMCA}/k_{s*}) should also be a large order of magnitude, similar to Λ. We hence rescale them to extract the lone large parameter Λ and render all the parameters of order unity with respect to Λ:

$$\frac{k'}{k_{s*}} = k\Lambda \qquad \frac{g'}{C_* k_{s*}} = g\Lambda \qquad \frac{k'_{PMCA}}{k_{s*}} = k_{PMCA}\Lambda$$

where *k*, *g* and k_{PMCA} are now all unity order.

We get the dimensionless equation with a stiff dimensionless parameter and with dimensionless variables, time and parameters.

$$\frac{dC}{dt} = \Lambda \left[\frac{kC}{1 + \frac{C}{K_m} + \frac{C^2}{K_i}} + g - k_{PMCA} C - k_{NCX}(N_0 - N) e^{-\left(\frac{C - C_k}{k_a}\right)^2} \right]$$

$$\frac{dN}{dt} = 3k_{NCX}(N_0 - N) f(C) + d(N_0 - N) - k_s N$$

where the stiff parameter is $\Lambda = N_*/C_*$, then all the kinetic parameters *k, g,* $k_{PMCA,}$ and k_{NCX} are dimensionless and of unit order with respect to Λ.

Note, with this order assignment, we assume that *k'* >> k_s, $g' \gg C_* k_s$ and $k'_{PMCA} \gg k_s$ but $k'_{NCX} \sim k_s$, which is reasonable considering the high Calcium concentration spikes require large calcium fluxes, much larger than sodium fluxes. Also note that because of

663 the difference in equilibrium calcium and sodium concentrations, the NCX flux produces
664 large fraction change in the calcium concentrations but not the sodium concentrations.
665 This is the key to stiff dynamics with large Λ to allow the quasi-steady state nullcline
666 analysis. For Figure 4H, the parameters were chosen in arbitrary units, at $k = 3$, $\frac{1}{K_i} = 3$,
667 $\frac{1}{K_m} = 0.5$, $k_{PMCA} = 0.8$, $C_K = 0.6$, $k_{NCX} = 5$, $K_a = 0.35$, $k_s = 0.06$, $d = 0.2$, $g = 0.6$, and
668 $[Na]_{ext} = 32$. Initial conditions were set consistently at $[Na]_0 = 30$ and $[Ca]_0 = 0.7$.
669
670
671
672
673
674
675
676
677
678
679
680
681

Acknowledgements

We acknowledge support from the University of Notre Dame through “Advancing Our Vision” Initiative in Stem Cell Research and Bioengineering and Life Science Initiative, Harper Cancer Research Institute – American Cancer Society Institutional Research Grant (IRG-17-182-04), American Heart Association through Career Development Award (19-CDA-34630012 to D.H.-P.), National Science Foundation (2047903 and 2225601 to D.H-P., 2120200 to EMBRIO Institute), National Institutes of Health (R35-GM-143055 to D.H.-P. and R35-GM-156615 to J.Z.), National Science Foundation-Graduate Fellowships Program (NSF-GRFP to D.P.J.).

Conflict of interest statement: The authors have declared that no conflict of interest exists.

Author contributions: D.P.J., S.C., A.D., H-C.C., J.Z., and D.H.-P. conceived the ideas, designed the experiments, interpreted the data, and wrote the manuscript. D.P.J., K.M, and S.S. conducted the experiments and analyzed the data. S.C. and A.D. helped develop the computational models and analyzed the data. A.D., H-C.C., J.Z., and D.H.-P. supervised the study. All authors have approved the manuscript.

Data and Code Availability

The relevant imaging data are present in the **Supplementary Information** and **Supplementary Movies**. Raw images are deposited in FigShare. The original code used in this study can be found on Github Repository [https://github.com/donghyunjeong21/calcium_signaling].

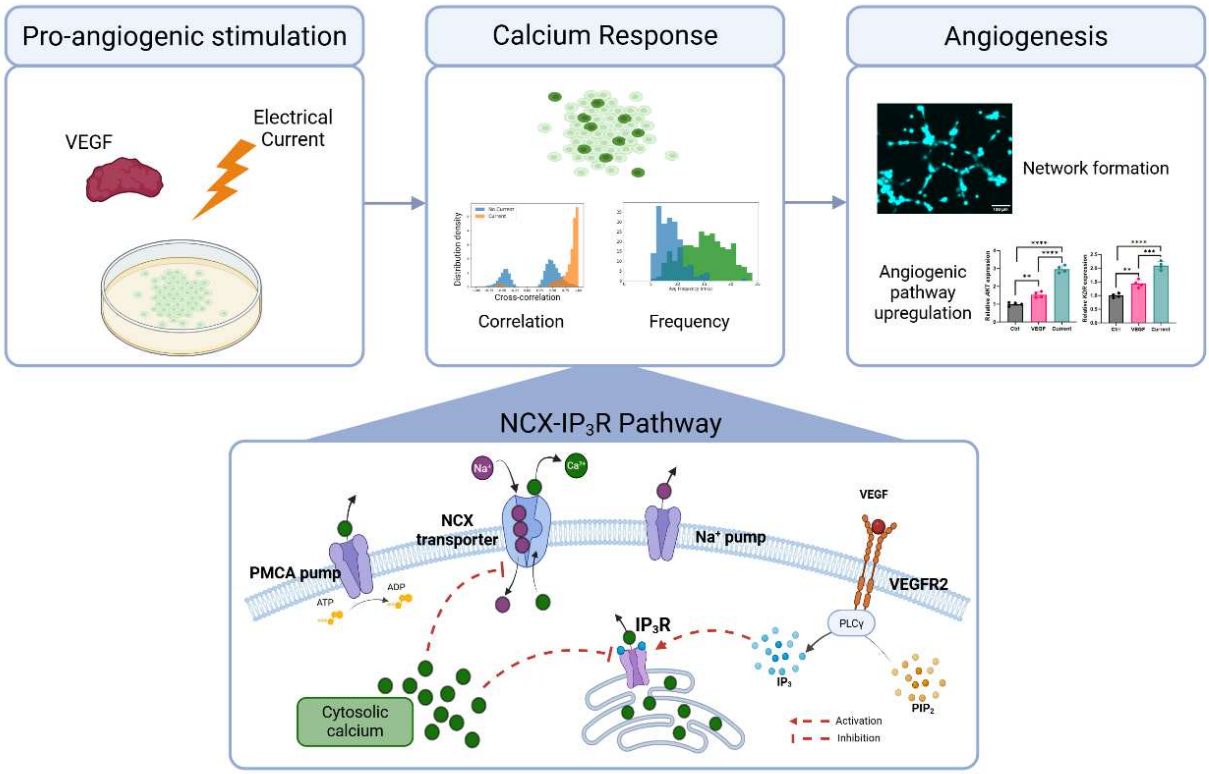


Figure 1. Calcium acts as the central pathway guiding angiogenesis. Cellular calcium activities in response to various external stimuli, such as VEGF stimulation. The cells modulate the correlation and frequency of the calcium spiking behavior in response to these stimuli through the NCX-IP3R pathway. These changes to calcium signaling translate to enhanced vascular network formation and upregulation of angiogenic pathways.

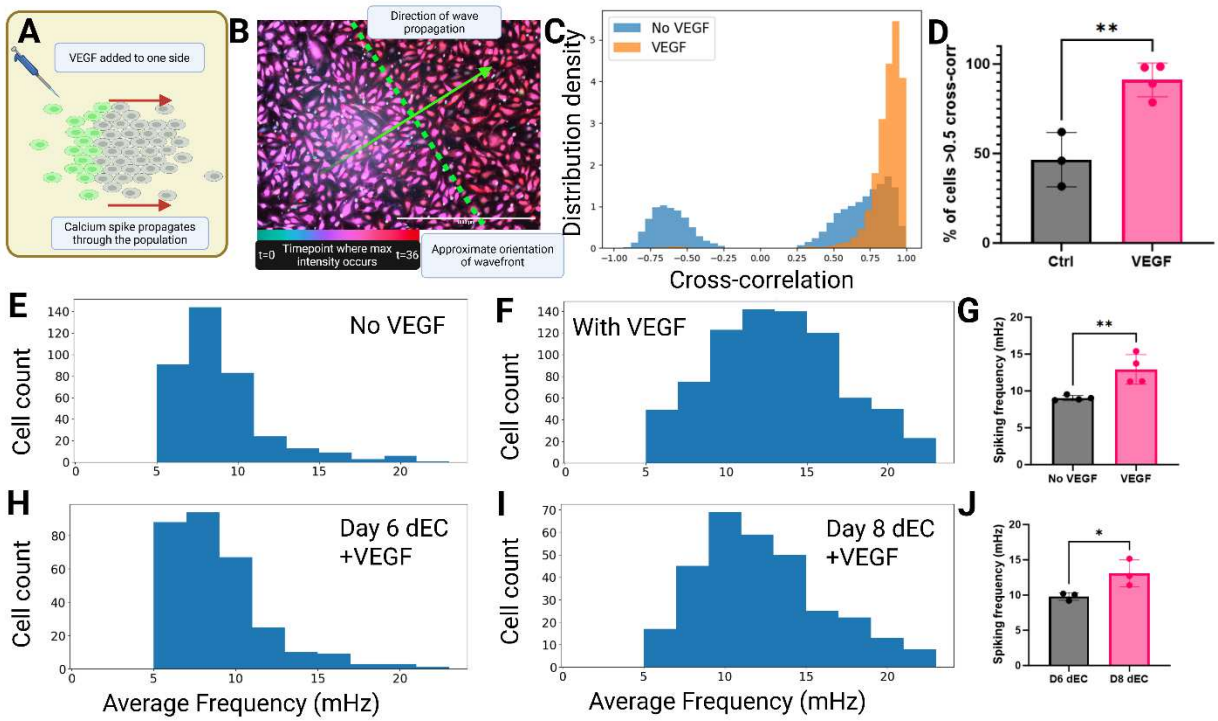
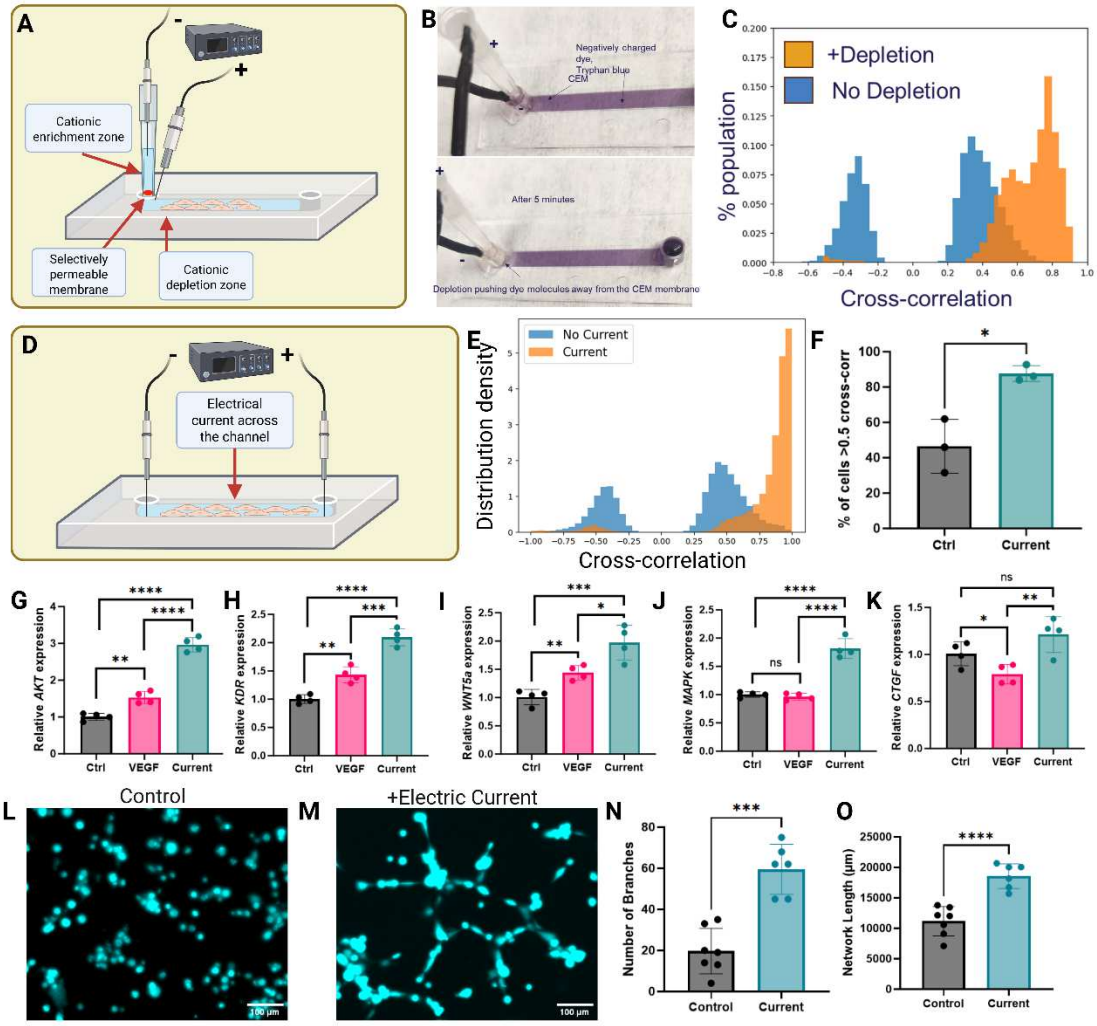


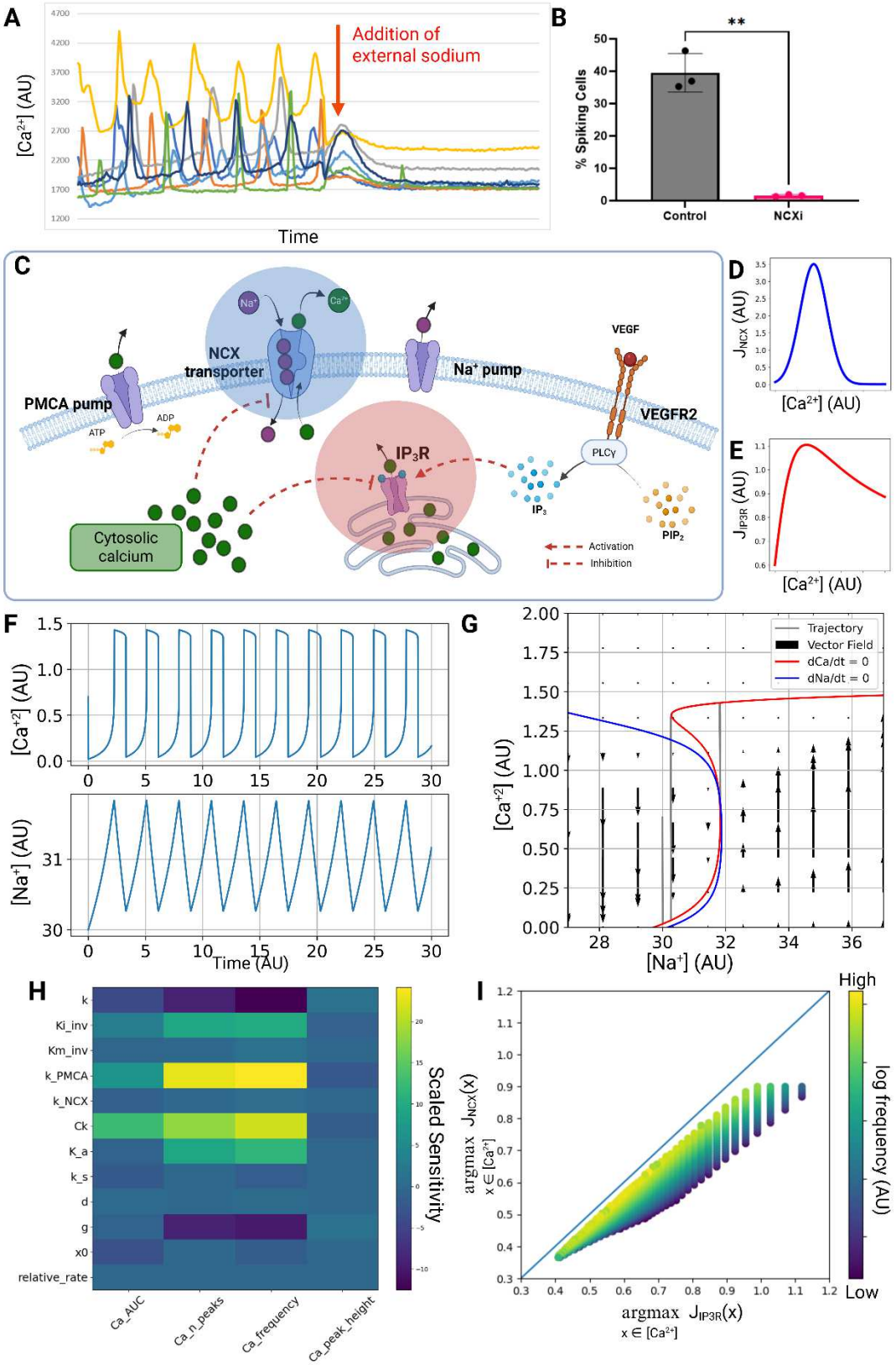
Figure 2. VEGF induces a frequency shift in calcium-oscillatory endothelial cell population. (A) Schematic of the VEGF-induced calcium wave propagation within seconds of adding VEGF. **(B).** Temporal color code image of the cells following the VEGF addition. The color corresponds to the timepoint at which the maximum intensity is reached. An approximate wavefront is shown in green dotted line, and the direction of wave propagation, which is perpendicular to the wavefront, is shown in green solid line. **(C).** Distribution density plot of the degree of cross-correlation for each cell-cell pair within the imaging window for VEGF and no-VEGF conditions. **(D).** Percentage of cell-cell pairings that exhibit higher than 0.5 in cross-correlation value, n=3 for control and n=4 for VEGF. **(E-F).** Histogram showing the distribution of average oscillation period in oscillatory cells cultured with and without VEGF. The cells with VEGF were subjected to 50ng/mL of VEGF for 24 hours. **(G).** Average spiking frequency of cells treated with and without VEGF, n=4. Each run was with the identical donor but cultured and measured independently. **H-I.** Average oscillation period histogram for iPSC-differentiated ECs at day 6 and day 8 of differentiation. Mean oscillation periods are shown on the top right for each plot. **J.** Average spiking frequency of iPSC-dEC at day 6 and 8, n=3 for both groups. *p<0.05, **p<0.01. Scale bar represents 1mm.



731

732 **Figure 3. VEGF or electrical stimulation induces intercellular calcium waves across**
733 **coupled endothelial cells. (A).** Schematic for the cation depletion setup, showing the
734 placement of a double-well with a selectively permeable membrane. **(B).** Demonstration
735 of the viability of the depletion chip showing the removal of negatively charged Tryphan
736 Blue dye after 5 minutes of applying the current. **(C).** Histogram showing the distribution
737 of degree of cross-correlation for each cell-cell pair before and after cationic depletion.
738 **(D).** Schematic of the current-induced transient ionic depletion in a microfluidic channel.
739 **(E).** Distribution density plot of the degree of cross-correlation with and without the current
740 applied. **(F).** Percentage of cell-cell pairings that exhibit higher than 0.5 in cross-
741 correlation value, n=3 for both groups. **(G-K).** Relative RNA expression level changes for

AKT, *KDR*, *WNT5a*, *MAPK*, and *CTGF* with VEGF treatment and current treatment normalized to the non-treated cells, run in technical replicates of n=4. **(L-M)** Representative images of tube formation results from current-treated and non-treated ECs on Matrigel. Scale bar represents 100 μm. **(N-O)** Quantification of the overall tube length and number of branches for the two EC conditions, quantified using Aututube. n = 5 for the current-treatment condition and n=6 for control. *p<0.05, **p<0.01, ***p<0.001, ****p<0.0001.


A
Addition of external sodium
[Ca2+] (AU)
Time
B
% Spiking Cells
Control
NCXi
**
C
NCX transporter
Na+ pump
PMCA pump
ADP
ATP
VEGF
VEGFR2
PLCγ
IP3R
IP3
PIP2
Cytosolic calcium
Activation
Inhibition
D
JNCX (AU)
[Ca2+] (AU)
E
JIP3R (AU)
[Ca2+] (AU)
F
[Ca+2] (AU)
[Na+] (AU)
Time (AU)
G
Trajectory
Vector Field
dCa/dt = 0
dNa/dt = 0
[Ca+2] (AU)
[Na+] (AU)
H
k
Ki_inv
Km_inv
k_PMCA
k_NCX
Ck
K_a
k_s
d
g
x0
relative_rate
Ca_AUC
Ca_n_peaks
Ca_frequency
Ca_peak_height
Scaled Sensitivity
I
High
Low
log frequency (AU)
argmax JNCX(x)
x ∈ [Ca2+]
argmax JIP3R(x)
x ∈ [Ca2+]

749

Figure 4. An IP_3R-NCX calcium oscillation model can produce calcium oscillatory system in non-excitable cell model. (A). Representative calcium intensity trace for one cell undergoing external sodium spike from 140 mM to 300 mM, which shows a sudden disappearance of all calcium oscillation activity, similar to calcium dynamics predicted in figure H. **(B).** Percentage of oscillatory cells when treated with 50 μM SEA0400 NCX inhibitor showing significant inhibition of oscillatory behavior, n=4. **p<0.01. **(C).** Diagram showing the proposed mechanism of NCX-IP_3R coupled calcium oscillatory system. The two key transporters with activation-inhibition curves with respect to calcium are highlighted with shaded circles. **(D-E).** Calcium flux of NCX and IP_3R transporters with respect to cytosolic calcium concentration showing maximum transport rates at similar calcium concentrations. **(F-G).** Simulated calcium and sodium oscillation and the associated nullclines on Ca-Na phase plane showing a single unstable equilibrium in the middle branch of the S-hysteresis. Calcium nullcline is shown in red, sodium nullcline is shown in blue. **(H).** Local feature sensitivity analysis of the model with respect to each parameter. Area under the curve (AUC), number of peaks, and frequency of the peaks for calcium are quantified for the sensitivity analysis. The values shown are for central difference analysis with ±1% perturbations. **(I).** Effect on the frequency of the oscillation of the calcium concentration at the maximum flux for IP_3R and NCX transporters. Color scheme corresponds to log of the frequency of the oscillation, while lack of points indicates a non-oscillatory system. Oscillation is only possible when the peak flux of IP_3R is achieved at a slightly higher calcium concentration compared to that of peak NCX flux.

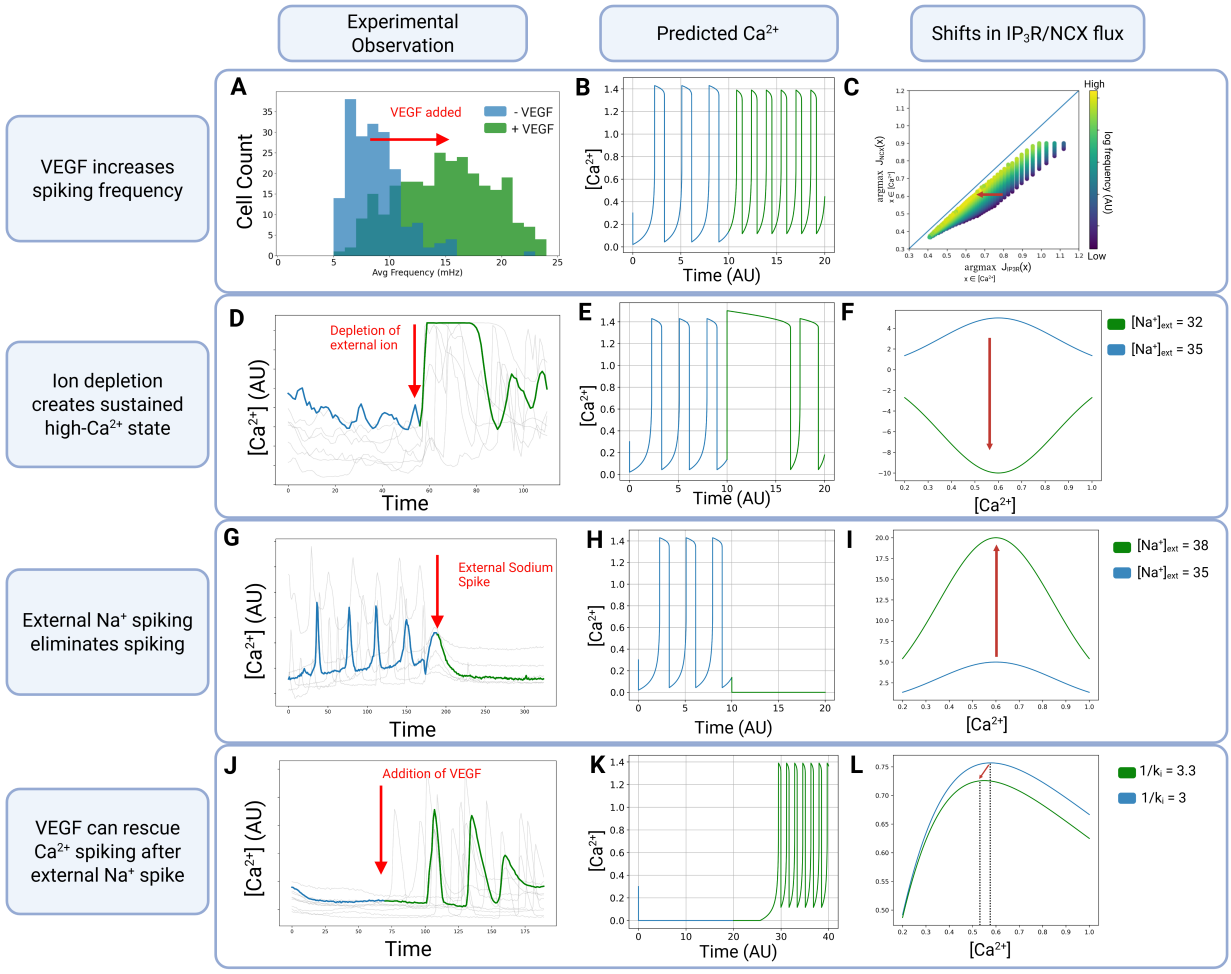


Figure 5. The NCX-IP$_3$R model predicts the effects of external perturbations on calcium oscillation patterns. (A). Overlaid histograms of the average oscillatory frequencies of ECs treated with and without VEGF, replicated from Figure 2. **(B).** Oscillatory traces and phase plots with the parameter shift of $1/K_i$ from 3 to 3.3 introduced at timepoint 25. **(C).** A shift in the K_i parameter that models VEGF response results in a leftward shift in the system from the low-frequency to the high-frequency region. The shift in the state is shown in red arrow. **(D).** Representative calcium concentration traces of several cells in a depletion setup which undergoes two rounds of depletion at the marked timepoints. During the depletion, cells exhibit a high calcium phase that is sustained for longer than a typical calcium oscillation peak. **(E).** Oscillatory traces and phase plots with the parameter shift of $[Na+]_{ext}$ from 32 to 28 introduced at timepoint 25. **(F).** J_{NCX} curves as a function of cytosolic calcium concentration before and after external ion shift, in blue and green, respectively. The NCX curve is pushed into the negative indicating activation

of reverse mode. **(G).** Representative calcium concentration traces of several cells treated with sudden spike in external sodium concentration. Immediately following the addition of external sodium, all spiking activity ceases. **(H).** Oscillatory traces and phase plots with the parameter shift of $[Na^+]_{ext}$ from 32 to 38 introduced at timepoint 25. **(I).** J_{NCX} curves as a function of cytosolic calcium concentration before and after external ion shift, in blue and green, respectively. The increased external sodium concentration increases the maximum flux of NCX, leading to the upward shift of the curve. **(J).** Representative calcium concentration traces of several cells which have been exposed to high external sodium concentration for several minutes before VEGF was introduced. The timepoint at which VEGF is added is marked with the red arrow. Sodium concentration remains at 300mM throughout the entire time. **(K).** Oscillatory traces and phase plots with the $[Na^+]_{ext}$ set to 36 and 1/Ki parameter shifted from 3 to 3.3 at timepoint 35. **(L).** J_{IP3R} curves as a function of cytosolic calcium concentration before and after VEGF, in blue and green, respectively. The reduction in the K_i parameter results in a leftward shift of the peak of the curve indicating a lowered threshold for IP3R-calcium release. For all figures except C, blue represents pre-perturbation and green represents post-perturbation.

References

1. Berridge MJ. Calcium signalling and cell proliferation. *BioEssays*. 1995;17(6):491-500. doi:10.1002/bies.950170605
2. Dejos C, Gkika D, Cantelmo AR. The Two-Way Relationship Between Calcium and Metabolism in Cancer. *Front Cell Dev Biol*. 2020;8:573747. doi:10.3389/fcell.2020.573747
3. Trebak M, Kinet JP. Calcium signalling in T cells. *Nat Rev Immunol*. 2019;19(3):154-169. doi:10.1038/s41577-018-0110-7
4. Tsai FC, Seki A, Yang HW, et al. A polarized Ca2+, diacylglycerol and STIM1 signalling system regulates directed cell migration. *Nat Cell Biol*. 2014;16(2):133-144. doi:10.1038/ncb2906
5. Egelman DM, Read Montague P. Calcium Dynamics in the Extracellular Space of Mammalian Neural Tissue. *Biophysical Journal*. 1999;76(4):1856-1867. doi:10.1016/S0006-3495(99)77345-5
6. Raffaello A, Mammucari C, Gherardi G, Rizzuto R. Calcium at the Center of Cell Signaling: Interplay between Endoplasmic Reticulum, Mitochondria, and Lysosomes. *Trends in Biochemical Sciences*. 2016;41(12):1035-1049. doi:10.1016/j.tibs.2016.09.001
7. Berridge MJ, Lipp P, Bootman MD. The versatility and universality of calcium signalling. *Nat Rev Mol Cell Biol*. 2000;1(1):11-21. doi:10.1038/35036035
8. Brodskiy PA, Zartman JJ. Calcium as a signal integrator in developing epithelial tissues. *Phys Biol*. 2018;15(5):051001. doi:10.1088/1478-3975/aabb18
9. Boulware MJ, Marchant JS. Timing in Cellular Ca2+ Signaling. *Current Biology*. 2008;18(17):R769-R776. doi:10.1016/j.cub.2008.07.018
10. Yadav V, Chong N, Ellis B, et al. Constant-potential environment for activating and synchronizing cardiomyocyte colonies with on-chip ion-depleting perm-selective membranes. *Lab Chip*. 2020;20(22):4273-4284. doi:10.1039/D0LC00809E
11. De Marco G, Lomartire A, Manera U, et al. Effects of intracellular calcium accumulation on proteins encoded by the major genes underlying amyotrophic lateral sclerosis. *Sci Rep*. 2022;12(1):395. doi:10.1038/s41598-021-04267-8
12. Grynkiewicz G, Poenie M, Tsien RY. A new generation of Ca2+ indicators with greatly improved fluorescence properties. *J Biol Chem*. 1985;260(6):3440-3450.
13. Brodskiy PA, Wu Q, Soundarrajan DK, et al. Decoding Calcium Signaling Dynamics during Drosophila Wing Disc Development. *Biophysical Journal*. 2019;116(4):725-740. doi:10.1016/j.bpj.2019.01.007
14. Soundarrajan DK, Huizar FJ, Paravitorghabeh R, Robinett T, Zartman JJ. From spikes to intercellular waves: Tuning intercellular calcium signaling dynamics modulates organ size control. Haugh JM, ed. *PLoS Comput Biol*. 2021;17(11):e1009543. doi:10.1371/journal.pcbi.1009543
15. McCarron JG, Lee MD, Wilson C. The Endothelium Solves Problems That Endothelial Cells Do Not Know Exist. *Trends in Pharmacological Sciences*. 2017;38(4):322-338. doi:10.1016/j.tips.2017.01.008
16. Zandrini T, Florczak S, Levato R, Ovsianikov A. Breaking the resolution limits of 3D bioprinting: future opportunities and present challenges. *Trends in Biotechnology*. 2023;41(5):604-614. doi:10.1016/j.tibtech.2022.10.009
17. Zhu W, Qu X, Zhu J, et al. Direct 3D bioprinting of prevascularized tissue constructs with complex microarchitecture. *Biomaterials*. 2017;124:106-115. doi:10.1016/j.biomaterials.2017.01.042
18. Duan J, Fang Y, Tian Y, Wang Z, Yang B, Xiong Z. 3D Bioprinting of Prevascularized Bone Organoids for Rapid In Situ Cranial Bone Reconstruction. *Adv Healthcare Materials*. 2025;14(16):2501376. doi:10.1002/adhm.202501376

19. Hanjaya-Putra D, Wong KT, Hirotsu K, Khetan S, Burdick JA, Gerecht S. Spatial control of cell-mediated degradation to regulate vasculogenesis and angiogenesis in hyaluronan hydrogels. *Biomaterials*. 2012;33(26):6123-6131. doi:https://doi.org/10.1016/j.biomaterials.2012.05.027
20. Alderfer L, Saha S, Fan F, Wu J, Littlepage LE, Hanjaya-Putra D. Multi-parameter tunable synthetic matrix for engineering lymphatic vessels. *Communications Biology*. 2024;7(1):1262. doi:10.1038/s42003-024-06935-7
21. Hanjaya-Putra D, Bose V, Shen YI, et al. Controlled activation of morphogenesis to generate a functional human microvasculature in a synthetic matrix. *Blood*. 2011;118(3):804 LP - 815.
22. Fan F, Su B, Kolodychak A, et al. Hyaluronic Acid Hydrogels with Phototunable Supramolecular Cross-Linking for Spatially Controlled Lymphatic Tube Formation. *ACS Appl Mater Interfaces*. 2023;15(50):58181-58195. doi:10.1021/acsami.3c12514
23. Hakeem RM, Subramanian BC, Hockenberry MA, et al. A Photopolymerized Hydrogel System with Dual Stiffness Gradients Reveals Distinct Actomyosin-Based Mechano-Responses in Fibroblast Durotaxis. *ACS Nano*. 2023;17(1):197-211. doi:10.1021/acsnano.2c05941
24. Meissner S, Raos B, Svirskis D. Hydrogels can control the presentation of growth factors and thereby improve their efficacy in tissue engineering. *European Journal of Pharmaceutics and Biopharmaceutics*. 2022;181:1-21. doi:10.1016/j.ejpb.2022.10.021
25. Su J, Song Y, Zhu Z, et al. Cell–cell communication: new insights and clinical implications. *Sig Transduct Target Ther*. 2024;9(1):196. doi:10.1038/s41392-024-01888-z
26. Schröter C, Stapornwongkul KS, Trivedi V. Local cellular interactions during the self-organization of stem cells. *Current Opinion in Cell Biology*. 2023;85:102261. doi:10.1016/j.ceb.2023.102261
27. Montes D, Saha S, Taglione A, et al. Tuning the Morphological Properties of Granular Hydrogels to Control Lymphatic Capillary Formation. *Advanced Materials Interfaces*. 2025;12(14):2401037. doi:10.1002/admi.202401037
28. Hong SG, Ashby JW, Kennelly JP, et al. Mechanosensitive membrane domains regulate calcium entry in arterial endothelial cells to protect against inflammation. *J Clin Invest*. 2024;134(13). doi:10.1172/JCI175057
29. Ando J, Komatsuda T, Kamiya A. Cytoplasmic calcium response to fluid shear stress in cultured vascular endothelial cells. *In Vitro Cell Dev Biol*. 1988;24(9):871-877. doi:10.1007/BF02623896
30. Jafarnejad M, Cromer WE, Kaunas RR, Zhang SL, Zawieja DC, Moore JE. Measurement of shear stress-mediated intracellular calcium dynamics in human dermal lymphatic endothelial cells. *American Journal of Physiology-Heart and Circulatory Physiology*. 2015;308(7):H697-H706. doi:10.1152/ajpheart.00744.2014
31. Surya VN, Michalaki E, Fuller GG, Dunn AR. Lymphatic endothelial cell calcium pulses are sensitive to spatial gradients in wall shear stress. Mogilner A, ed. *MBoC*. 2019;30(7):923-931. doi:10.1091/mbc.E18-10-0618
32. Hu Q, Ziegelstein RC. Hypoxia/Reoxygenation Stimulates Intracellular Calcium Oscillations in Human Aortic Endothelial Cells. *Circulation*. 2000;102(20):2541-2547. doi:10.1161/01.CIR.102.20.2541
33. Yokota Y, Nakajima H, Wakayama Y, et al. Endothelial Ca2+ oscillations reflect VEGFR signaling-regulated angiogenic capacity in vivo. *eLife*. 2015;4:e08817. doi:10.7554/eLife.08817
34. Dawson NS, Zawieja DC, Wu MH, et al. Signaling pathways mediating $VEGF_{165}$ -induced calcium transients and membrane depolarization in human endothelial cells. *FASEB j*. 2006;20(7):991-993. doi:10.1096/fj.05-3923fje
35. Hanjaya-Putra D, Yee J, Ceci D, Truitt R, Yee D, Gerecht S. Vascular endothelial growth factor and substrate mechanics regulate in vitro tubulogenesis of endothelial progenitor cells. *J Cell Mol Med*. 2010;14(10):2436-2447. doi:10.1111/j.1582-4934.2009.00981.x

36. Dragoni S, Reforgiato M, Zuccolo E, et al. Dysregulation of VEGF-induced proangiogenic Ca2+ oscillations in primary myelofibrosis-derived endothelial colony-forming cells. *Experimental Hematology*. 2015;43(12):1019-1030.e3. doi:10.1016/j.exphem.2015.09.002
37. Kusuma S, Shen YI, Hanjaya-Putra D, Mali P, Cheng L, Gerecht S. Self-organized vascular networks from human pluripotent stem cells in a synthetic matrix. *Proceedings of the National Academy of Sciences*. 2013;110(31):12601-12606. doi:10.1073/pnas.1306562110
38. Patsch C, Challet-Meylan L, Thoma EC, et al. Generation of vascular endothelial and smooth muscle cells from human pluripotent stem cells. *Nature Cell Biology*. 2015;17:994.
39. Harding A, Cortez-Toledo E, Magner NL, et al. Highly Efficient Differentiation of Endothelial Cells from Pluripotent Stem Cells Requires the MAPK and the PI3K Pathways. *Stem Cells*. 2017;35(4):909-919. doi:10.1002/stem.2577
40. Yadav V, Senapati S, Chang HC. Ion-Depleting Action of Perm-Selective Membranes for Enhancing Electrical Communication and Gated Ion Channel Activity in Cell Cultures. *ACS Biomater Sci Eng*. 2022;8(11):4618-4621. doi:10.1021/acsbiomaterials.1c01384
41. He Y, Sun MM, Zhang GG, et al. Targeting PI3K/Akt signal transduction for cancer therapy. *Sig Transduct Target Ther*. 2021;6(1):425. doi:10.1038/s41392-021-00828-5
42. Trinh XB, Tjalma WAA, Vermeulen PB, et al. The VEGF pathway and the AKT/mTOR/p70S6K1 signalling pathway in human epithelial ovarian cancer. *Br J Cancer*. 2009;100(6):971-978. doi:10.1038/sj.bjc.6604921
43. Glaviano A, Foo ASC, Lam HY, et al. PI3K/AKT/mTOR signaling transduction pathway and targeted therapies in cancer. *Mol Cancer*. 2023;22(1):138. doi:10.1186/s12943-023-01827-6
44. Abid MdR, Guo S, Minami T, et al. Vascular Endothelial Growth Factor Activates PI3K/Akt/Forkhead Signaling in Endothelial Cells. *ATVB*. 2004;24(2):294-300. doi:10.1161/01.ATV.0000110502.10593.06
45. Gerber HP, McMurtrey A, Kowalski J, et al. Vascular Endothelial Growth Factor Regulates Endothelial Cell Survival through the Phosphatidylinositol 3′-Kinase/Akt Signal Transduction Pathway. *Journal of Biological Chemistry*. 1998;273(46):30336-30343. doi:10.1074/jbc.273.46.30336
46. Masckauchán TNH, Agalliu D, Vorontchikhina M, et al. Wnt5a signaling induces proliferation and survival of endothelial cells in vitro and expression of MMP-1 and Tie-2. *Mol Biol Cell*. 2006;17(12):5163-5172. doi:10.1091/mbc.e06-04-0320
47. Coupe N, Guo L, Bridges E, et al. WNT5A-ROR2 axis mediates VEGF dependence of BRAF mutant melanoma. *Cell Oncol*. 2023;46(2):391-407. doi:10.1007/s13402-022-00757-7
48. Modi SJ, Kulkarni VM. Vascular Endothelial Growth Factor Receptor (VEGFR-2)/KDR Inhibitors: Medicinal Chemistry Perspective. *Medicine in Drug Discovery*. 2019;2:100009. doi:10.1016/j.medidd.2019.100009
49. Wang X, Bove AM, Simone G, Ma B. Molecular Bases of VEGFR-2-Mediated Physiological Function and Pathological Role. *Front Cell Dev Biol*. 2020;8:599281. doi:10.3389/fcell.2020.599281
50. Wagner MJ, Lyons YA, Siedel JH, et al. Combined VEGFR and MAPK pathway inhibition in angiosarcoma. *Sci Rep*. 2021;11(1):9362. doi:10.1038/s41598-021-88703-9
51. Niimi Y. PKC- and MAPK-independent upregulation of VEGF receptor expressions in human umbilical venous endothelial cells following VEGF stimulation. *Hepatology Research*. 2001;21(3):261-267. doi:10.1016/S1386-6346(01)00091-2
52. Inoki I, Shiomi T, Hashimoto G, et al. Connective tissue growth factor binds vascular endothelial growth factor (VEGF) and inhibits VEGF-induced angiogenesis. *The FASEB Journal*. 2002;16(2):1-27. doi:10.1096/fj.01-0332fje
53. Francescone Iii RA, Faibish M, Shao R. A Matrigel-Based Tube Formation Assay to Assess the Vasculogenic Activity of Tumor Cells. *JoVE*. 2011;(55):3040. doi:10.3791/3040

54. Montoya-Zegarra JA, Russo E, Runge P, et al. AutoTube: a novel software for the automated morphometric analysis of vascular networks in tissues. *Angiogenesis*. 2019;22(2):223-236. doi:10.1007/s10456-018-9652-3
55. Ten Tusscher KHWJ, Noble D, Noble PJ, Panfilov AV. A model for human ventricular tissue. *American Journal of Physiology-Heart and Circulatory Physiology*. 2004;286(4):H1573-H1589. doi:10.1152/ajpheart.00794.2003
56. FitzHugh R. Impulses and Physiological States in Theoretical Models of Nerve Membrane. *Biophysical Journal*. 1961;1(6):445-466. doi:10.1016/S0006-3495(61)86902-6
57. Purves D, Augustine G, Fitzpatrick D. The Ionic Basis of the Resting Membrane Potential. In: *Neuroscience. 2nd Edition.* Sinauer Associates; 2001.
58. Enyedi P, Czirják G. Molecular Background of Leak K^+ Currents: Two-Pore Domain Potassium Channels. *Physiological Reviews*. 2010;90(2):559-605. doi:10.1152/physrev.00029.2009
59. Strazzullo P, Leclercq C. Sodium. *Advances in Nutrition*. 2014;5(2):188-190. doi:10.3945/an.113.005215
60. Watanabe T. Electrochemical signaling mechanism in cardiac muscle. In: *Modeling Electrochemical Dynamics and Signaling Mechanisms in Excitable Cells with Pathological Case Studies*. Elsevier; 2022:149-166. doi:10.1016/B978-0-323-98803-2.00001-8
61. Wang J, Zhang Z, Hu Y, et al. SEA0400, a novel Na+/Ca2+ exchanger inhibitor, reduces calcium overload induced by ischemia and reperfusion in mouse ventricular myocytes. *Physiol Res*. Published online 2007:17-23. doi:10.33549/physiolres.930894
62. Marchant JS, Taylor CW. Rapid Activation and Partial Inactivation of Inositol Trisphosphate Receptors by Inositol Trisphosphate. *Biochemistry*. 1998;37(33):11524-11533. doi:10.1021/bi980808k
63. Hajnoczky G. Minimal requirements for calcium oscillations driven by the IP3 receptor. *The EMBO Journal*. 1997;16(12):3533-3543. doi:10.1093/emboj/16.12.3533
64. Bezprozvanny I, Ehrlich BE. The inositol 1,4,5-trisphosphate (InsP3) receptor. *J Membarin Biol*. 1995;145(3). doi:10.1007/BF00232713
65. Patel S, Joseph SK, Thomas AP. Molecular properties of inositol 1,4,5-trisphosphate receptors. *Cell Calcium*. 1999;25(3):247-264. doi:10.1054/ceca.1999.0021
66. Taylor CW. Inositol trisphosphate receptors: Ca2+-modulated intracellular Ca2+ channels. *Biochimica et Biophysica Acta (BBA) - Molecular and Cell Biology of Lipids*. 1998;1436(1-2):19-33. doi:10.1016/S0005-2760(98)00122-2
67. Wagner LE, Joseph SK, Yule DI. Regulation of single inositol 1,4,5-trisphosphate receptor channel activity by protein kinase A phosphorylation. *J Physiol*. 2008;586(15):3577-3596. doi:10.1113/jphysiol.2008.152314
68. Noble D, Herchuelz A. Role of Na/Ca exchange and the plasma membrane Ca^{2+} -ATPase in cell function: Conference on Na/Ca Exchange. *EMBO Reports*. 2007;8(3):228-232. doi:10.1038/sj.embor.7400914
69. Weber CR, Ginsburg KS, Philipson KD, Shannon TR, Bers DM. Allosteric Regulation of Na/Ca Exchange Current by Cytosolic Ca in Intact Cardiac Myocytes. *The Journal of General Physiology*. 2001;117(2):119-132. doi:10.1085/jgp.117.2.119
70. Giladi M, Khananshvili D. Molecular Determinants of Allosteric Regulation in NCX Proteins. In: Annunziato L, ed. *Sodium Calcium Exchange: A Growing Spectrum of Pathophysiological Implications*. Vol 961. Advances in Experimental Medicine and Biology. Springer US; 2013:35-48. doi:10.1007/978-1-4614-4756-6_4
71. Giladi M, Lee SY, Ariely Y, et al. Structure-based dynamic arrays in regulatory domains of sodium-calcium exchanger (NCX) isoforms. *Sci Rep*. 2017;7(1):993. doi:10.1038/s41598-017-01102-x
72. Maack C, Ganesan A, Sidor A, O'Rourke B. Cardiac sodium-calcium exchanger is regulated by allosteric calcium and exchanger inhibitory peptide at distinct sites. *Circ Res*. 2005;96(1):91-99. doi:10.1161/01.RES.0000151334.48676.68

73. Araújo IM, Carreira BP, Pereira T, et al. Changes in calcium dynamics following the reversal of the sodium-calcium exchanger have a key role in AMPA receptor-mediated neurodegeneration via calpain activation in hippocampal neurons. *Cell Death Differ*. 2007;14(9):1635-1646. doi:10.1038/sj.cdd.4402171
74. Bano D, Young KW, Guerin CJ, et al. Cleavage of the Plasma Membrane Na+/Ca2+ Exchanger in Excitotoxicity. *Cell*. 2005;120(2):275-285. doi:10.1016/j.cell.2004.11.049
75. Schmitz EA, Takahashi H, Karakas E. Structural basis for activation and gating of IP3 receptors. *Nat Commun*. 2022;13(1):1408. doi:10.1038/s41467-022-29073-2
76. Andrikopoulos P, Baba A, Matsuda T, Djamgoz MBA, Yaqoob MM, Eccles SA. Ca2+ Influx through Reverse Mode Na+/Ca2+ Exchange Is Critical for Vascular Endothelial Growth Factor-mediated Extracellular Signal-regulated Kinase (ERK) 1/2 Activation and Angiogenic Functions of Human Endothelial Cells. *Journal of Biological Chemistry*. 2011;286(44):37919-37931. doi:10.1074/jbc.M111.251777
77. Brodskiy PA, Zartman JJ. Calcium as a signal integrator in developing epithelial tissues. *Phys Biol*. 2018;15(5):051001. doi:10.1088/1478-3975/aabb18
78. Thomas AP, Bird GStJ, Hajnóczky G, Robb-Gaspers LD, Putney JW. Spatial and temporal aspects of cellular calcium signaling. *The FASEB Journal*. 1996;10(13):1505-1517. doi:10.1096/fasebj.10.13.8940296
79. Berridge MJ, Bootman MD, Roderick HL. Calcium signalling: dynamics, homeostasis and remodelling. *Nat Rev Mol Cell Biol*. 2003;4(7):517-529. doi:10.1038/nrm1155
80. Moccia F, Brunetti V, Soda T, Berra-Romani R, Scarpellino G. Cracking the Endothelial Calcium (Ca2+) Code: A Matter of Timing and Spacing. *Int J Mol Sci*. 2023;24(23):16765. doi:10.3390/ijms242316765
81. Debir B, Meaney C, Kohandel M, Unlu MB. The role of calcium oscillations in the phenotype selection in endothelial cells. *Sci Rep*. 2021;11(1):23781. doi:10.1038/s41598-021-02720-2
82. Noren DP, Chou WH, Lee SH, et al. Endothelial cells decode VEGF-mediated Ca^{2+} signaling patterns to produce distinct functional responses. *Sci Signal*. 2016;9(416). doi:10.1126/scisignal.aad3188
83. Sun MY, Geyer M, Komarova YA. IP3 receptor signaling and endothelial barrier function. *Cell Mol Life Sci*. 2017;74(22):4189-4207. doi:10.1007/s00018-017-2624-8
84. Teubl M, Groschner K, Kohlwein SD, Mayer B, Schmidt K. Na+/Ca2+ Exchange Facilitates Ca2+-dependent Activation of Endothelial Nitric-oxide Synthase. *Journal of Biological Chemistry*. 1999;274(41):29529-29535. doi:10.1074/jbc.274.41.29529
85. Toussaint F, Charbel C, Blanchette A, Ledoux J. CaMKII regulates intracellular Ca2+ dynamics in native endothelial cells. *Cell Calcium*. 2015;58(3):275-285. doi:10.1016/j.ceca.2015.06.005
86. Sun MY, Geyer M, Komarova YA. IP3 receptor signaling and endothelial barrier function. *Cell Mol Life Sci*. 2017;74(22):4189-4207. doi:10.1007/s00018-017-2624-8
87. Ramshani Z, Fan F, Wei A, et al. A multiplexed immuno-sensor for on-line and automated monitoring of tissue culture protein biomarkers. *Talanta*. 2021;225:122021. doi:10.1016/j.talanta.2020.122021
88. Brini M, Carafoli E. The plasma membrane Ca^2+ ATPase and the plasma membrane sodium calcium exchanger cooperate in the regulation of cell calcium. *Cold Spring Harb Perspect Biol*. 2011;3(2):a004168. doi:10.1101/cshperspect.a004168
89. Cavalié A, Zimmermann R. Editorial: The evolving picture of Ca2+ leak from endoplasmic reticulum in health and diseases. *Front Physiol*. 2023;14:1182455. doi:10.3389/fphys.2023.1182455
90. Barmashenko G, Kockskämper J, Glitsch HG. Depolarization increases the apparent affinity of the Na+-K+ pump to cytoplasmic Na+ in isolated guinea-pig ventricular myocytes. *J Physiol*. 1999;517 (Pt 3)(Pt 3):691-698. doi:10.1111/j.1469-7793.1999.0691s.x

91. Yan Y, Wang L, Xue J, Chang HC. Ion current rectification inversion in conic nanopores: Nonequilibrium ion transport biased by ion selectivity and spatial asymmetry. *The Journal of Chemical Physics*. 2013;138(4):044706. doi:10.1063/1.4776216
92. Gadsby DC, Kimura J, Noma A. Voltage dependence of Na/K pump current in isolated heart cells. *Nature*. 1985;315(6014):63-65. doi:10.1038/315063a0
93. Stanley CM, Gagnon DG, Bernal A, Meyer DJ, Rosenthal JJ, Artigas P. Importance of the Voltage Dependence of Cardiac Na/K ATPase Isozymes. *Biophys J*. 2015;109(9):1852-1862. doi:10.1016/j.bpj.2015.09.015

Supplementary Files

This is a list of supplementary files associated with this preprint. Click to download.

- JeongetalSupplementaryInformation1.pdf
- SuppMovS8.mp4
- SuppMovS10.mp4
- SuppMovS12.avi
- SuppMovS11.mp4
- SuppMovS4.avi
- SuppMovS2.avi
- SuppMovS6.avi
- SuppMovS13.mp4
- SuppMovS1.avi
- SuppMovS7.avi
- SuppMovS9.mp4
- SuppMovS5.avi
- SuppMovS3.avi